Acta Materialia 186 (2020) 229–241

Contents lists available at ScienceDirect

Acta Materialia

journal homepage: www.elsevier.com/locate/actamat

Full length article

# On the observation of annealing twins during simulating β-grain refinement in Ti–6Al–4V high deposition rate AM with in-process deformation

J. Donoghue[a], A.E. Davis[a,*], C.S. Daniel[a], A. Garner[a], F. Martina[b], J. Quinta da Fonseca[a], P.B. Prangnell[a]

[a] Department of Materials, University of Manchester, MSS Tower, Manchester, M13 9PL, UK
[b] Welding Engineering and Laser Processing Centre, Cranfield University, Bedfordshire, MK43 0AL, UK

ARTICLE INFO

*Article History:*
Received 28 September 2019
Revised 2 December 2019
Accepted 6 January 2020
Available online 8 January 2020

*Keywords:*
Additive manufacture
Titanium
Grain size
Recrystallization
Texture

ABSTRACT

Additive Manufacture (AM) of Ti–6Al–4V frequently leads to undesirable, coarse, columnar β-grain structures with a strong <100> fibre texture. In Wire-Arc AM (WAAM), it has been found that the application of a low plastic strain, by methods such as inter-pass rolling, can disrupt β columnar growth and produce a refined, equiaxed grain structure that is more randomly orientated. The origin of this desirable effect has been investigated by thermo-mechanical simulation, direct in-situ EBSD observation, as well as by real-time synchrotron X-ray diffraction (SXRD) during rapid heating. These complementary approaches have shown that, when starting with a WAAM microstructure, the grain refinement process produces a unique micro-texture represented by a four-pole motif symmetrically centred on the parent grain {100} orientations. These new β-grain orientations can be reproduced by a double {112}<111> twinning operation, which produces 12 new, unique, β-orientation variants. High-resolution orientation-mapping techniques and in-situ SXRD heating simulations suggest that the prior β does not twin during deformation, but rather the grain refinement and related texture may be caused by annealing twinning during β re-growth on rapid re-heating of the deformed AM microstructure. Although this is the first time such a unique texture has been observed in a deformed and β annealed Ti–6Al–4V material, it was only found to dominate under the unusual conditions that occur in AM of rapid heating – a fine, lightly deformed $\alpha$ transformation microstructure, with a very coarse starting β-grain structure.

Crown Copyright © 2020 Published by Elsevier Ltd on behalf of Acta Materialia Inc. This is an open access article under the CC BY license. (http://creativecommons.org/licenses/by/4.0/)

## 1. Introduction

Additive manufacture (AM) is increasingly being embraced by the aerospace industry for producing high added-value components owing to its ability to fabricate near-net shape parts with shorter lead times. The advantages of AM are more significant in low volume manufacturing of titanium aerospace components, due to the inherently high material, tooling, and machining costs [1]. However, to economically produce large airframe parts requires high deposition rates of kilograms per hour and build envelopes of several meters. Directed energy deposition (DED) wire-fed AM processes are suitable for such applications because of their high material efficiency and productivity [2–4]. Wire-based processes under development include; laser [5] and E-beam based technologies (NASA, Sciaky™ [6,7]), and Wire-Arc Additive Manufacturing (WAAM) (e.g., Cranfield University, Norsk Titanium [8–12]). All of these processes employ a directed heat source and have melt pool sizes 2–10 mm wide, with a layer height of 1–2 mm [3–10,13]. The large melt pool results in lower solidification and cooling rates than found in conventional powder bed systems [13–17], which can cause substantially greater heterogeneity and anisotropy in finished components (e.g. [8,14,18–20]).

The formation of coarse columnar β-grain structures in AM with Ti–6Al–4V (Ti64) arises as a result of combining the melt pool solidification conditions with intrinsic metallurgical behaviour. In AM, the heated and translated melt pool creates steep thermal gradients at the solidification front. In addition, as well as remelting a proportion of the previously deposited layer, it raises the temperature of the material below the fusion boundary to above the β transus (which for Ti64 is ~ 1000°C [21,22]). Because the main alloying elements in Ti64 have a partition coefficient close to one [23], and there are no inoculants, the steep thermal gradients at the solidification front give rise to a narrow 'mushy' zone with insufficient supercooling to enable nucleation ahead of the solidification front [24]. Solidification,

* Corresponding author.
*E-mail address:* alec.davis@manchester.ac.uk (A.E. Davis).

https://doi.org/10.1016/j.actamat.2020.01.009
1359-6454/Crown Copyright © 2020 Published by Elsevier Ltd on behalf of Acta Materialia Inc. This is an open access article under the CC BY license. (http://creativecommons.org/licenses/by/4.0/)

therefore, occurs epitaxially from the remelted β grains at the fusion boundary that first re-grow on re-heating above the β transus from the residual β retained in the transformation microstructure from the previous deposition pass. As this cycle is repeated with every layer of deposition, the β grains can potentially grow continuously through the entire height of a build. In addition, due to the <100> preferential growth direction for solidification in BCC metals [25], competitive growth normal to the solidification front [26–28] typically results in a strong <100> fibre texture with the axis orientated close to normal to the deposited layers and tilted towards the heat source travel direction [8,18].

After deposition of each layer, transformation on cooling weakens the parent β texture as each $\alpha$ lath can adopt any one of the 12 possible orientations dictated by the Burgers orientation relationship (BOR) [29]. Nevertheless, the coarse directional parent-grain structure still leads to micro-$\alpha$ texture heterogeneity and mechanical anisotropy. Reducing the coarse β-grain size is therefore desirable in AM with Ti64 and can be achieved by both metallurgical means, or by thermomechanical processing. Traditional thermomechanical processing of Ti64 billets normally involves significant plastic deformation in order to break up the prior β structure, with the deformation taking place at high temperatures to accommodate the high strains required of 50–70% [30]. However, it has been recently shown in the WAAM process that only a moderate level of cold deformation, applied in-process by inter-pass rolling, is required to break up the columnar β-grain structure [31]. Originally this approach was investigated to reduce the build-up of residual stresses in AM deposits [12,31,32], but in Ti64 it has lead to a surprisingly high degree of β-grain refinement. Various rolling strategies have been explored, including applying profiled rollers and side rolling [31]. In all cases this produces a heterogeneous strain distribution within the deposit. However, a substantial reduction in β-grain size has been observed in built parts despite the modest level of strain experienced by the material [8,18,33]. For example, in WAAM parts, the application of only an 8% nominal plastic strain imparted by a roller on each added layer reduced the prior β-grain size from cm-long columnar grains to 140 $\mu$m diameter equiaxed grains; and a 19% reduction decreased the grain size further to 90 $\mu$m [18]. The microstructures and bulk textures from this study are reproduced in Fig. 1 (taken from [18]). Importantly, this high level of grain refinement and the resultant weakened texture has been shown to produce more isotropic tensile properties in AM parts [33].

Here, we have adopted several complimentary experimental approaches in order to better understand the origin of the high level of β-grain refinement and texture randomisation that can be produced by the application of small, cold, inter-pass, plastic strains to Ti64 in DED AM. This has included: simulating the deformation and heating steps in the inter-pass rolled WAAM process using plane-strain compression (PSC) and rapid heating, and examining the behaviour of individual large prior-β grains ex-situ by electron backscatter diffraction (EBSD) and in-situ heating in 'real-time' using synchrotron X-ray diffraction (SXRD). The original in-situ SEM heating experiment performed in Ref. [27] has also been repeated using a much larger sample area and to a higher temperature (just below the β transus). By studying the re-growth of the β phase in-situ and in real time, we have thus been able to track the development of the new β orientations generated during a typical simulated rolling-integrated WAAM deposition cycle. This work has confirmed the development of a unique β micro-texture on annealing, represented by a four-pole motif symmetrically centred on the parent grain {100} orientations, within each coarse parent β grain. These in-situ studies have been combined with modelling of the crystallographic relationships between the parent and new β orientations, and high resolution orientation mapping of the as-deformed material using both transmission Kikuchi diffraction (TKD) and scanning precession electron diffraction (SPED). The results have been used to propose the most plausible explanation for both the highly effective grain refinement and the unique micro-texture that has been found to form under the unusual combination of rapid heating and the fine, lightly cold-deformed starting $\alpha$ microstructures experienced in a wire-fed DED process with inter-pass deformation.

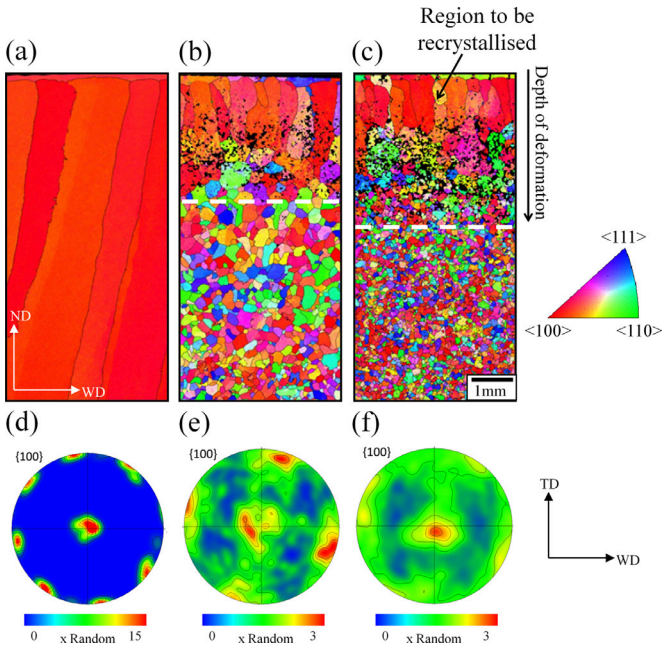



**Fig. 1.** Reconstructed β-phase EBSD maps (IPF colouring with respect to the build direction) and {100} pole figures from (a) unrolled WAAM wall, and walls produced with inter-pass rolling applied using loads of (b) 50 kN and (c) 75 kN. Directions are defined as: WD ≡ parallel to the wall length, TD ≡ transverse direction normal to the wall surface, and ND ≡ direction normal to deposited layers. The dashed white lines indicate the depth of the deformation zone from the last rolling pass that would recrystallise during a subsequent deposition pass, which can be identified from areas of lower indexing. Note: the different texture intensities in the unrolled and rolled walls. The figure is adapted from [18]. (For interpretation of the references to colour in this figure legend, the reader is referred to the web version of this article.)

## 2. Experimental methods

### 2.1. WAAM samples

For this study, single track ~6 mm wide linear walls were built with a pulsed gas tungsten arc welding system using a constant heat source travel direction. Full details can be found elsewhere in Refs. [8,32]. The walls were deposited on a Ti64 base plate using a high laminar flow rate trailing argon shielding device to avoid oxidation, with a 1.2 mm Ti64 alloy welding wire and an average current of 110 A. Inter-pass deformation of each added layer was achieved by running a roller across the top of the walls, after each deposition pass, using a rigid gantry system. The 100 mm roller contained a 3.6 mm radius semi-circular groove to match the bead profile of the top of the wall. The compressive load was applied downwards through the roller bearings and controlled by a load cell. For the deformed walls, a rolling load of 50 or 75 kN was applied after every layer of deposition once the temperature of the top layer had cooled to room temperature. The sample reference frame used throughout is defined here as: WD is the heat source travel direction parallel to each wall (or the 'welding' direction), TD is the transverse direction, and ND the build height direction normal to each layer.

### 2.2. Process simulation

#### 2.2.1. Rolling simulation

It was observed previously [18] that applying a single roller to the top of a single pass wide WAAM wall predominantly produced lateral spreading in TD and negligible elongation along the wall in WD, so approximate PSC conditions were met as:

$\varepsilon_{TD} \approx -\varepsilon_{ND}$ and $\varepsilon_{WD} \sim 0$

However, due to the different constraint in WAAM inter-pass rolling, the plane strain is rotated by 90° relative to that found in traditional sheet rolling, where elongation occurs in the rolling direction (WD // RD) and there is negligible strain in the transverse direction (TD).

In order to replicate the PSC conditions, a channel die compression rig was designed with a 5 mm channel width, as shown in Fig. 2. Samples were coated with graphite lubrication and were strained at room temperature at a fixed cross-head speed of 30 mm $s^{-1}$ (which is similar to that experienced in the process) to an average reduction of ~ 15%. This amount of strain was comparable to that for the rolling-integrated WAAM walls which can experience an average height reduction of 8–19% (see Table 1). The plane strain compression samples were cut from an undeformed WAAM wall, which had a coarse β-grain structure (Fig. 1(a)) and were compressed with the same grain orientation as in the rolled walls; i.e., with their build direction (ND) as the compression axis, which was approximately parallel to the direction of columnar grain growth. Two sets of samples were used: 20 mm long by 5 mm in cross-section to produce longer 'matchstick' specimens for rapid heating in an electrothermal mechanical testing system (ETMT), and 5 mm cubes to produce samples for the SEM in-chamber heating experiments. The samples produced for analysis, with their measured net plastic strains, are summarised in Table 1 along with the heating rates used in the different simulations.

#### 2.2.2. Thermal cycle simulation

An Instron® ETMT8800 thermal-mechanical simulator was used to replicate the rapid temperature cycle experienced in the WAAM process by each deposited and rolled layer when it is re-heated above the β transus, by the heat input arising from deposition of the next layer. The ETMT machine allowed rapid, resistive heating to be performed on miniature specimens with the temperature controlled by a type-R thermocouple spot-welded to the sample [34]. 20 mm long matchstick samples were machined from the centre of the longer PSC samples with a cross section of 1.9 × 1.9 mm, as shown in Fig. 2(b). The gauge length was held at 12 mm, leaving 4 mm to be gripped at each end by the water cooled grips to ensure good electrical contact, as shown in Fig. 2(c). The heating rate used was based on the work of [8,22], where thermocouples were plunged into the WAAM melt pool and it was found that typical heating rates reached on re-heating each layer through the transus temperature by the subsequent deposition pass were ~ 500°C $s^{-1}$. The peak temperature used was chosen to be 1080°C to ensure that a significant section of the 12 mm gauge length was taken above the β-transus temperature (~1000°C [22]), but not so high as to cause excessive grain growth. Rapid cooling of the samples (~ 100°C $s^{-1}$), again similar to that seen in the WAAM process, was also ensured by conduction to the water-cooled grips. To investigate the β-grain transformation behaviour induced by a slower heating rate, a similar sample was also heated in a Carbolite rapid-heating furnace with a heating rate of 2.3°C $s^{-1}$. To mimic the temperature gradient through the β transus produced in the ETMT test, one sample end was insulated and the furnace heated to 1020°C until the 'hot' sample end reached this temperature.

### 2.3. In-situ *SEM heating experiment*

For the in-chamber SEM heating stage experiment, a small sample with dimensions 2 × 2 × 1 mm was cut from the most heavily deformed region of the rolled wall's last layer (i.e. that had not been re-heated) at a depth of ~ 2 mm below the top surface [18]. This sample had an initial large, columnar β-grain structure. Following standard metallographic preparation techniques, the sample was adhered to a Gatan Murano heating stage using a water-based carbon paste, left to air dry for 2 h, and then baked for 2 h at 93°C and 2 h at 260°C. EBSD mapping at temperature was carried out in an FEI Nova 600 NanoLab SEM fitted with an Oxford instruments Nordlys Max$^2$ EBSD detector with Oxford Instruments' AZtec acquisition software.

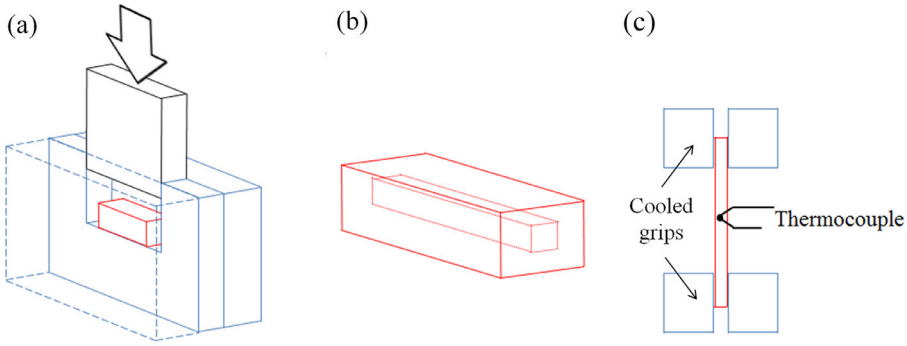



**Fig. 2.** Schematic diagram of the three main steps used in simulation of the WAAM-rolling process: (a) PSC of a sample cut from an undeformed WAAM wall, (b) location of the ETMT sample cut from the PSC WAAM sample, and (c) ETMT experimental setup for reproducing the rapid thermal cycle, with a temperature gradient through the β transus, induced by the next layer of addition.

**Table 1**
Dimensions and plastic strains of the rolling-integrated WAAM wall and plane strain compression (PSC) WAAM samples used to simulate the inter-pass rolling process, with the heating rates used in the various experiments. All PSC samples were machined from an un-deformed WAAM wall, with a large β-grain size, and deformed in a channel die tool with the compression axis parallel to the build direction ND.

| Experiment | Sample dimensions [mm] | Average sample strain $\varepsilon_{ND}$ | Heating rate [°C $s^{-1}$] |
|---|---|---|---|
| In-situ SEM – WAAM rolled wall (75 kN load) | 2 × 2 × 1 | −0.19 | 2.3 with 50°C increments |
| ETMT – rapid heating (SXRD) | 5 × 5 × 20 | −0.14 | ~ 500 |
| Furnace – slow heating | 5 × 5 × 20 | −0.12 | 2.3 |

The temperature was measured indirectly by a thermocouple attached to the heating stage.

The sample was gradually heated through the $\alpha$-β transformation taking EBSD maps every 50°C, from 800°C to 950°C, with an area of ~ 1 $mm^2$, to observe the transformation. Each map took ~ 15 min to complete after the stage temperature and microstructure were allowed to stabilise for 15 min, so this experiment represented a stepped heating response with a very slow average heating rate of 0.028°C $s^{-1}$. Previous in-chamber SEM heating experiments [27] found that transformation to β reached only ~ 35% at a measured temperature of 950°C, which was much less than would be predicted for the Ti64 alloy. Suppression of the transformation was attributed to absorption of remnant chamber gases into the sample surface which stabilised the $\alpha$ phase. In the current work, this was prevented by attaching a small cube of Zr to the heating stage close to the Ti64 sample to preferentially absorb the remnant chamber gases. This technique produced a significant increase in the fraction of β phase observed at each mapping temperature, which was closely in line with that expected from the β approach curve [22]. For example, the β volume fraction at a stage temperature of 950°C was measured to be 93% by EBSD.

### 2.4. In-situ *synchrotron X-Ray diffraction*

Synchrotron X-ray diffraction (SXRD) measurements were recorded in transmission mode at the Diamond Light Source on the I12:JEEP (Joint Engineering, Environmental and Processing) beam line. Matchstick samples prepared for ETMT (§2.2) were illuminated with an 89 keV monochromatic beam, covering a gauge volume of 0.5 × 0.5 × 1.9 mm with the sample-detector distance set at ~ 1200 mm. Full diffraction pattern rings were continuously recorded using a high-resolution two-dimensional (2-D) Pixium detector, at a 10 Hz acquisition frequency, whilst a rapid temperature rise was applied to the sample using direct-current resistive heating in an ETMT rig positioned within the beam line, with a heating rate of ~ 500°C $s^{-1}$. The synchrotron diffraction data was analysed using the Data Analysis Workbench (DAWN) software package [35,36], with the intensity variations around each of the individual $\alpha$ and β lattice-plane diffraction rings determined and plotted against azimuthal angle, to monitor the appearance of new grain orientations. Additionally, a full azimuthal integration was applied to each of the patterns to produce intensity versus $2\theta$ plots, which were then analysed using Rietveld refinement in the TOPAS software package [37] for determination of the relative $\alpha$/β volume fraction from each pattern. Unfortunately, the measured temperature data was deemed unreliable, so temperatures used in figures were estimated from CALPHAD calculations of the $\alpha$ and β phase fractions using equilibrium phase diagrams from the thermodynamic modelling software package JMatPro.

### 2.5. *EBSD analysis and* β*-phase reconstruction*

Prior and post-heating mapping of the Ti64 samples were performed with a step size of 2 $\mu$m using a CamScan Maxim FEG-SEM or an FEI Sirion FEG-SEM operated with a 20 kV accelerating voltage. Orientation maps were collected with an Oxford instruments NordlysNano EBSD system using AZtec HKL™ acquisition software. Large area maps of half of the ETMT and furnace-heated sample were obtained, measuring 13.0 × 1.9 mm, in order to acquire orientation data across the whole sample area from the hot central region (taken above the β transus) to that cooled by water grips or insulation. The EBSD maps are presented in either inverse pole figure (IPF) colouring relative to the build direction (ND), or in Euler colouring, depending on which colouring better presented the desired map features.

Due to the low β volume fraction at room temperature (~ 5–9% [38]) and its fine distribution in the WAAM samples, it was not feasible to determine the high-temperature β-grain structure by directly mapping the residual β. To characterise the β grains in the ex-situ samples and in-situ starting microstructures, the β phase was reconstructed using the procedure developed by Davies and Wynne [39,40], based on work by Humbert et al. [41,42]. This technique is explained fully in [39] and exploits the BOR to calculate the 6 possible orientations of the prior β phase, and then selects the most probable solution by comparing possible parent β orientations for neighbouring $\alpha$ laths. During this procedure, $\alpha$ points were defined to belong to the same variant within a 2° misorientation spread. A divergence of up to 3° from the BOR was accepted for $\alpha$ variants to be considered as part of the same parent β grain.

### 2.6. *High-resolution orientation mapping*

To attempt to study the deformation structure in the retained β at room temperature, two higher-resolution orientation-mapping techniques were employed: (i) transmission Kikuchi diffraction (TKD) using an FEI Magellan 400L SEM operated at 30 kV, whereby an electron transparent sample is tilted 20° away from the detector and Kikuchi diffraction patterns are detected in transmission [43]; and (ii) using scanning precession electron diffraction (SPED) in an FEI Tecnai F30 transmission electron microscope (TEM), which exploits template matching of diffraction spot patterns using the Nanomegas ASTAR system [44]. The TEM in this case was operated at 300 kV, with a focused probe diameter of 3 nm and an optimised precession angle of 0.8°. The lamella used for both high-resolution orientation-mapping techniques was prepared using the standard in-situ FIB lift-out technique using an FEI Quanta 3D FIB.

## 3. Results

### 3.1. Ex-situ *EBSD analysis of the simulated deformed WAAM samples*

A reconstructed-β EBSD map of a PSC deformed matchstick sample after rapid heating in the ETMT is shown in Fig. 3(a). The upper section that was reheated above the β transus had a refined, equiaxed grain structure, in comparison to the coarse columnar parent β grains found in the original undeformed WAAM wall, which can still be seen in the bottom section of the sample. It can be noted that this simulated sample looks very similar in appearance to the real interpass rolled WAAM wall shown in Fig. 1(c). However, the 14% deformation imparted to the sample in the PSC die and rapid heating has led to a slightly finer β-grain diameter of ~ 50 $\mu$m, compared to 90 $\mu$m [18] in the actual WAAM wall (Fig. 1), presumably because the average temperature rise in the β-annealed region of the heat affected zone is higher in the WAAM process, causing greater grain growth. As the strain across the length of the PSC sample was approximately homogenous, the transition to the original parent columnar grains seen at the ends of the ETMT specimen can be attributed to cooling by the grips, which prevented the temperature rising sufficiently for the growth of any new β orientations.

Although PSC deformation and rapid re-heating above the β transus gave rise to a uniform, fine, equiaxed grain structure, comprised predominantly of high-misorientation boundaries, it can be seen that the bulk texture in Fig. 4(a) is not entirely random and shows a distribution of <100> poles tilted approximately 30° away from the build direction ($z$). Additionally, in the maps in Fig. 3(a), it is possible to identify clustering in the IPF colouring. For example, in region 4 at the upper right of the map in Fig. 3(b), there is a prevalence of blue-coloured grains. Different regions identified by their distinctly different local micro-texture and the boundaries between each region, separated on this basis, have been numbered in Fig. 3(b), along with the {100} pole figure obtained from each region. When examined individually, it can be seen that the pole figures for each distinct micro-texture region exhibit the same unusual intensity motif centred on {100} pole positions, which are rotated relative to

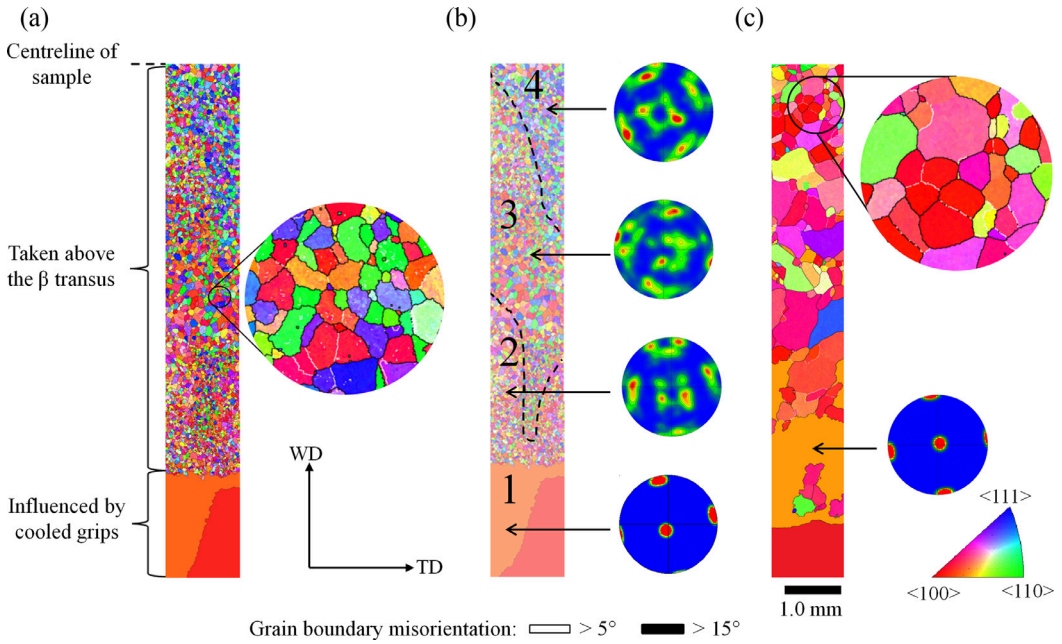



**Fig. 3.** Reconstructed β orientation maps of the simulated ETMT and furnace-heated samples incorporating {100} pole figures of highlighted regions: (a) the rapidly-heated sample with the relevant locations on the sample marked in (b), and (c) the slowly-heated sample. Maps are given in IPF colouring with respect to the build direction.

each other from region to region. This unusual motif (not previously reported in Ti alloys) consists of a four-pole spread of orientations arranged symmetrically around a central point that has four-fold symmetry. It can also be noted that the shape of the micro-texture regions are strongly reminiscent of the coarse original β-grain structure seen in the starting material.

The above inference can be readily confirmed as the unrecrystallised prior β grains still remained in the cooler sample ends, and these large columnar grains can be assumed to have originally continued some distance up into the hotter region of the sample. The 'before and after' rapid heating micro-textures can therefore be directly compared for the same parent β grain for regions 1 and 2 in Fig. 3(b) as has been shown more fully in Fig. 5. In this figure, the {100} pole figure for the prior β orientation (grain 1) reveals that there is a direct relationship between the original β orientation and the resultant refined-β texture found in the same grain when re-heated above the β transus in region 2. From comparison of these two regions, it can be clearly seen that the four-pole intensity motif of the refined grains is symmetrically centred around the {100} poles of the parent β orientation. In Fig. 3(b), this motif, although still centred on {100} symmetry, is rotated in regions 3 and 4 because they originated from different parent columnar β grains that were present prior to recrystallisation. Thus, it is evident that the micro-texture of the refined grains is not random and is closely related to that of their parent β-grain orientations. As the refined β grains originated from several (~ 4) parent coarse β grains, the bulk texture (shown in Fig. 4) is weaker and the strong relationship between each parent grain and its recrystallised micro-texture is less apparent.

A furnace simulation was also performed at a much lower heating rate of 2.3°C $s^{-1}$ on another PSC deformed sample to compare directly with the interesting micro-texture discussed above. It can be seen in Fig. 3(c), that when using a much lower heating rate of 2.3°C $s^{-1}$ the average grain diameter produced (262 $\mu$m) was five times larger than recorded in the WAAM simulation with rapid heating. In addition, the microstructure contained a higher proportion of low angle grain boundaries – or subgrains – compared to the rapidly-heated sample, so it can be considered to be partially 'recrystallised'. The prior parent β-grain structure was also less apparent in the slow heating rate sample and was difficult to discern from the local texture variation since fewer grains could be sampled. However, the bulk

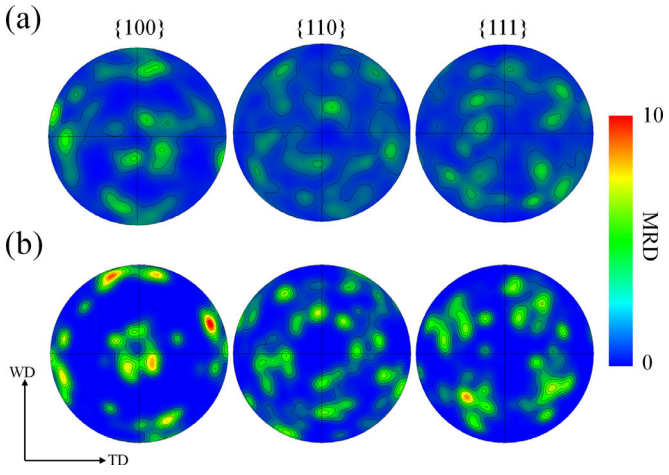



**Fig. 4.** Bulk β textures obtained from the whole matchstick samples for the (a) rapidly-heated condition in Fig. 3(a), and (b) slowly-heated sample in Fig. 3(c).

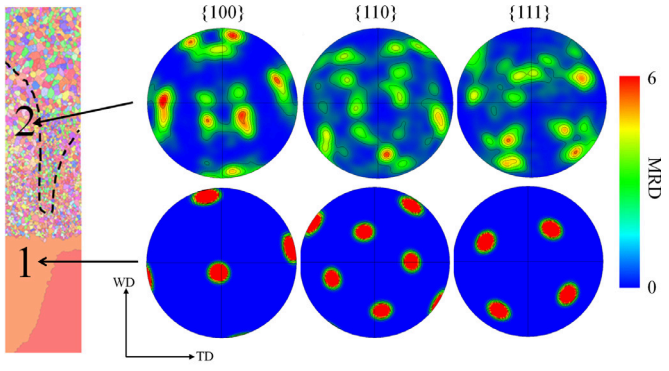



**Fig. 5.** Direct comparison of the reconstructed 'before and after' rapid annealing β micro-textures (marked '1' and '2' in Fig. 3(b)) obtained from the same parent β grain in the ETMT sample with gradient heating.

texture {100} pole figure of the partially recrystallised region (Fig. 4 (b)) also showed a four-pole motif similar to that found in the rapidly heated sample micro-textures, where the <100> poles are tilted ~ 30° away from the build direction with four-fold symmetry, and this is probably because, in this case, there was one large dominant β parent grain within the small sample volume analysed.

### 3.2. In-situ *synchrotron X-ray diffraction*

Real-time, rapid-heating simulations using WAAM-equivalent heating rates of 500°C $s^{-1}$ were also performed in the I12:JEEP Diamond beam line, using an ETMT matchstick sample machined from a WAAM PSC sample deformed to 14% strain. The results from this experiment are summarised in Figs. 6 and 7. In Fig. 6, $\alpha$ and β phase integrated azimuthal angle versus intensity plots are provided with example diffraction patterns of interest obtained at increasing temperatures. Diffraction patterns were collected with a frequency of 10 Hz, which represented a temperature increase during each pattern acquisition of only 50°C at this high heating rate. The diffraction data obtained in the SXRD experiment has been summarised in Fig. 7(a) by plotting the measured peak intensities as a function of the β volume fraction measured from the SXRD data. It should be noted that in the small 0.5 × 0.5 × 1.9 mm gauge volume analysed, there was only one β orientation present before heating, and this experiment

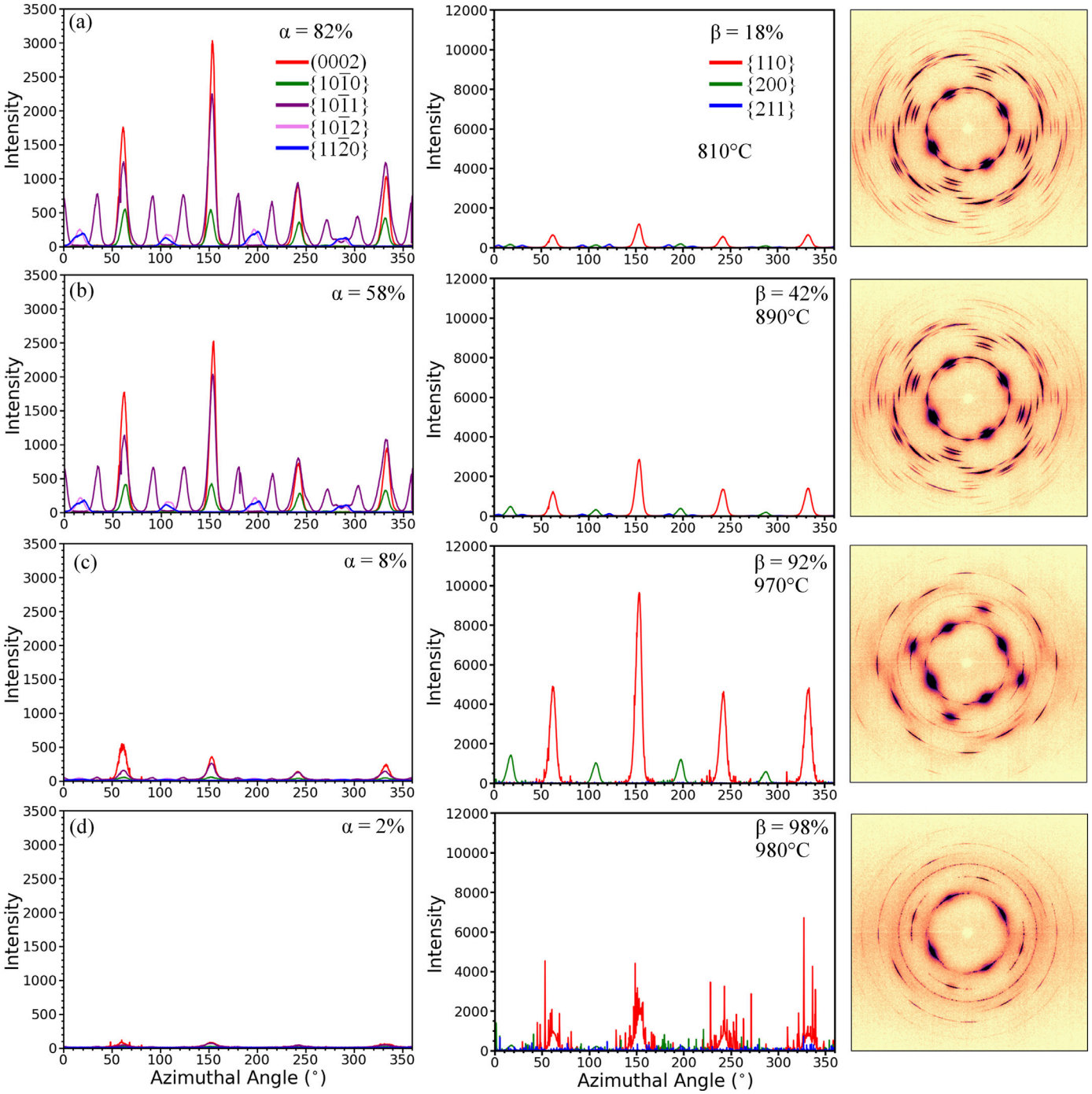



**Fig. 6.** $\alpha$ (left) and β phase (right) azimuthal angle intensity plots and example diffraction patterns from the in-situ rapid heating SXRD experiment (heating rate ~ 500°C $s^{-1}$, sample rate 10 Hz). Temperatures were estimated from CALPHAD calculations of the $\alpha$ and β phase fractions using the JMatPro thermodyanic modelling package.

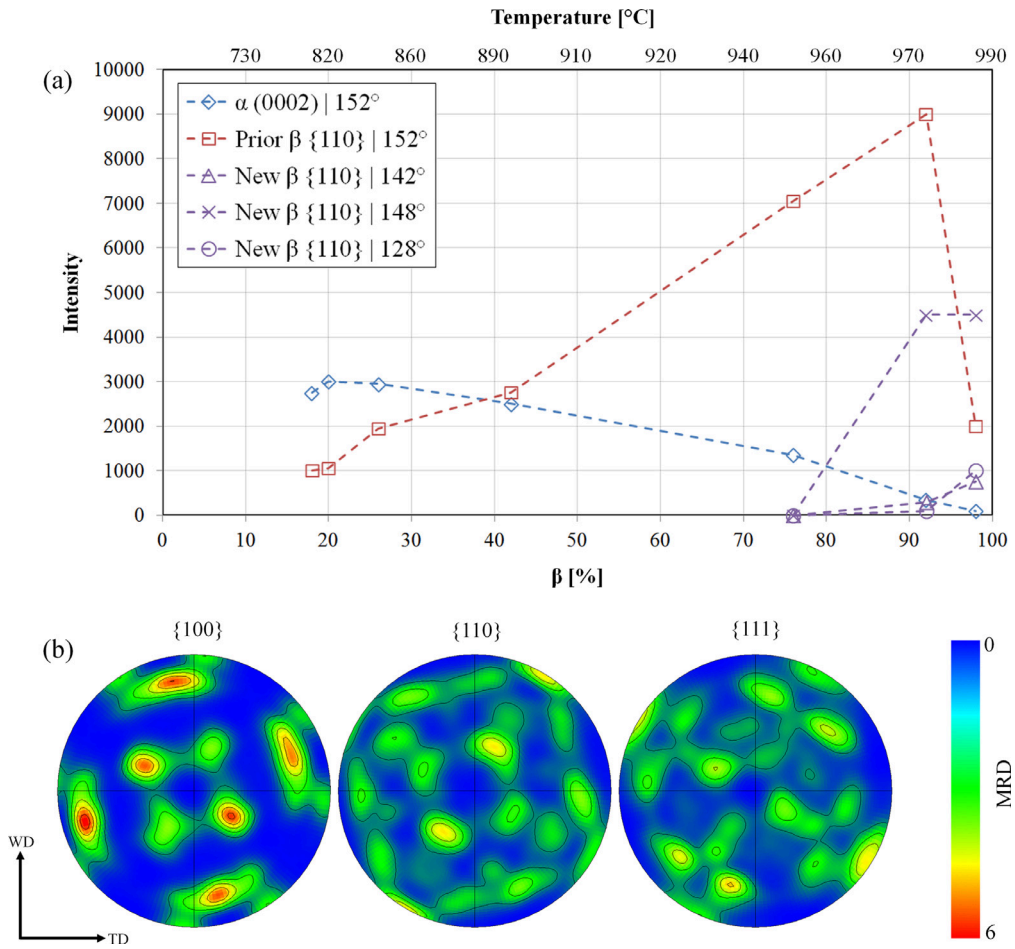



**Fig. 7.** (a) A summary of the SXRD in-situ rapid-heating experiment results showing selected single diffraction-peak intensities for $\alpha$, the prior deformed β grain, and a selection of the new β grain orientation peaks, plotted against percent β transformed. In (b), the reconstructed-β texture obtained from an EBSD map of the gauge volume after the SXRD rapid-heating experiment is shown. Temperatures were estimated from CALPHAD calculations of the $\alpha$ and β phase fractions using the JMatPro thermodyanic modelling package.

was therefore equivalent to rapidly re-heating a single parent β crystal that transformed during cooling in the WAAM process, and was subsequently lightly cold-deformed before re-heating.

As the temperature increased through the β-transus approach curve, it can be seen in Figs. 6 and 7 that the diffraction peaks present from the single prior β orientation intensify first. This prior β grain was the sole orientation that could be identified for the majority of the $\alpha$ to β transformation, and it was only when 8% $\alpha$ remained that new β orientations were found in the spectrum. These new reflections also appeared within a limited range of ~ 30° either side of the prior β peaks. As the new β orientations first began to grow, with increasing temperature, the intensity of the prior parent β grain orientation first increased. More importantly, in the final stages of β re-growth, the intensity of the prior-β peak then started to suddenly decrease (Fig. 7(a)). For example, by a 98% β volume fraction, which is equivalent to just below the transus temperature, the peak intensities reduced to a fifth of that seen at 92% β, and many of the new orientations produced had more intense diffraction peaks than the original β orientation. It should be noted that no new orientations could be found in the β diffraction profiles for volume fractions below 76% (~ 850°C) or above 92% β, so it can be assumed that all the new β orientations appeared somewhere in the range of the later stage of the transus approach curve (i.e. as β re-grows) and then started to replace the original parent orientation when competitive growth became possible above the β transus.

Finally, after the experiment, the gauge volume was sectioned and mapped by EBSD. The reconstructed-β texture from this map is shown in Fig. 7(b) and again clearly depicts the same unique microtexture as shown in Fig. 5. In the recrystallised single β parent SXRD gauge volume, the intensity of the characteristic four-fold motif is even more symmetric than previously recorded.

### 3.3. In-situ *SEM-EBSD heating experiment*

In Fig. 8, results are presented from a sample taken from the last layer of the 75 kN rolled WAAM wall that was heated in-situ in the SEM chamber and EBSD mapped at 50°C temperature intervals from 800°C to 950°C. Fig. 8(a) shows the β reconstruction of the initial prior β-grain structure and Fig. 8(b)–(d) shows the subsequent evolution of this microstructure with increasing temperature. The latter orientation maps have been separated into the indexed $\alpha$ and β phases in order to better appreciate their response during β re-growth. As there was no appreciable evolution of the β orientations at lower temperatures, maps below 850°C have been omitted. At 850°C and 900°C (Fig. 8(b) and (c)), 10.6% and 42.5% of the indexed points had transformed to β, respectively. As the β re-grew, new orientations, or potential new β-grain nuclei, (i.e. regions significantly disorientated with respect to the parent β) can initially be seen to emerge at 900°C (arrowed in Fig. 8(c)) at prior β-grain boundaries, and within the prior β grains, although the number of new orientations were limited. On increasing the temperature to 950°C, the β volume fraction increased to 93% and the regions with new β orientations at the original β-grain boundaries grew, whereas the number of new β orientations seen within the prior β grains greatly diminished.

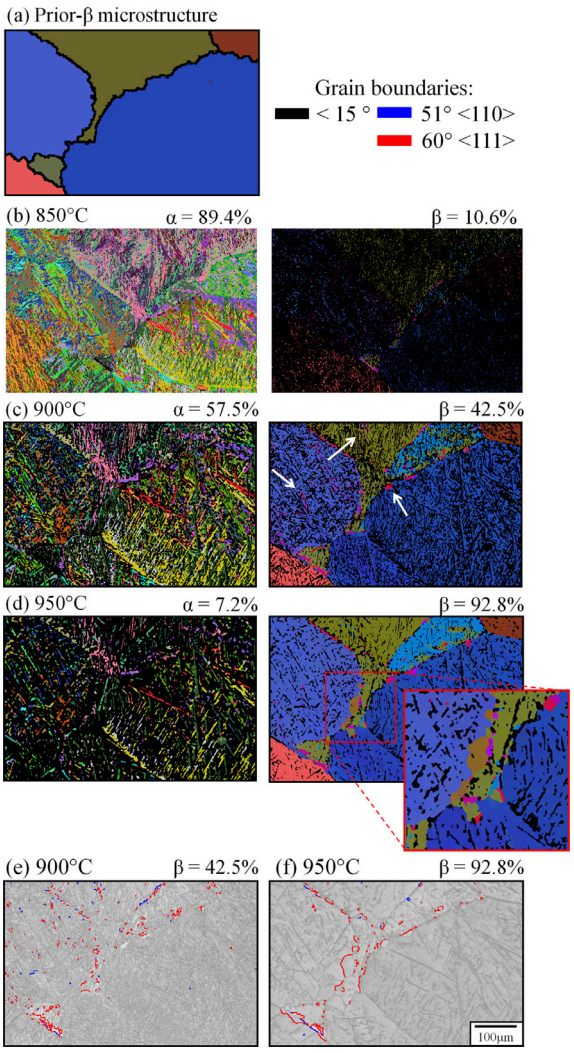



**Fig. 8.** Example EBSD maps in Euler colouring from the in-situ SEM heating experiment: (a) the reconstructed prior β-grain structure (with grain boundary misorientations of >15° highlighted), and separated $\alpha$ and β direct orientation maps obtained at (b) 850, (c) 900 (arrows indicate emerging β-grain nuclei), (d) 950°C. Band contrast maps with β-twin boundaries highlighted are shown for the β microstructures at (e) 900°C and (f) 950°C.

Overall, it can thus be seen that in this experiment, where the effective heating rate was very slow, the density of new nuclei that survived to 950°C was relatively low. However, special 51° <110> and 60° <111> β twin boundaries have also been highlighted in the pattern quality maps at 900 and 950°C in Fig. 8(e) and (f) where it can be noted that many of the new orientations are associated with 60° <111> twin boundaries. Their location is easier to resolve in the 950°C map, where they can be observed to delineate some of the interfaces of the new β orientated regions within the parent grain.

## 4. Discussion

Successful simulation of the inter-pass rolling step used in the integrated-rolling WAAM process has been achieved by a combination of PSC deformation and rapid re-heating above the β transus, in small matchstick samples that were obtained from a coarse-grained undeformed WAAM wall (Figs. 1 and 3(a)). These samples replicated a similar level of β-grain size refinement to that seen when deformation was applied to each added layer as an integral part of the WAAM build process [8,18,33]. However, a surprising observation from this study is that, although the refined equiaxed β-grain structure was replicated, and contained predominantly high angle grain boundaries and had a similar weakened bulk texture, a systematic correlation was found between its recrystallised micro-texture and the coarse parent β-grain orientations from which it developed. This texture was characterised by the presence of a four-pole motif centred symmetrically on the {100} pole positions inherited from the parent grain, where each new pole deviated by ~ 30° from the parent {100} pole position (Fig. 5).

In previous studies of the inter-pass rolling WAAM process, the application of cold-rolling strains of 8–19% to each added layer led to a refined prior β-grain diameter of 90–140 $\mu$m, whereas in the simulated process presented here (Fig. 3) the applied plastic strain of ~ 14% gave rise to a finer average prior β-grain diameter of around 50 $\mu$m [18]. This disparity can be explained by the lower peak temperature reached during the simulation, which was selected to be only slightly above the β transus at 1080°C; whereas in the WAAM process the majority of the refined zone would be re-heated to a greater temperature in the β-phase field, increasing the opportunity for grain coarsening. It is also apparent from the furnace heating simulation that, if a slow heating rate is used, the same refined β-grain structure is not achieved, as shown in Fig. 3(c), where – with a slower more conventional heating rate – a significantly coarser β-grain size was obtained.

The in-situ SEM experiment with stepped slow heating (Fig. 8) showed that the prior deformation had generated new β orientations that could potentially act as grain nuclei during β re-transformation and subsequent grain growth, but this occurred predominantly at prior β-grain boundaries. In addition, while new orientations were observed to form within the prior β grains at lower temperatures, they were largely unstable and consumed at temperatures above 950°C. This suggests that when a slow heating rate is used, the conditions required to form the high density of new, stable β-grain orientations required for a high level of grain refinement are not realised. This could be because, with a slow heating rate, the stored energy from deformation is reduced by recovery leaving only nucleation sites where plastic incompatibility (e.g. at prior β-grain boundaries) would be expected to cause the greatest level of local lattice rotation. Alternatively, the nuclei for the new grains seen in the rapid heating ex-situ ETMT experiment may not have all pre-existed in the deformed state, and another mechanism which generates new β orientations during re-heating could become important at high heating rates through the β-transus region.

The rapid heating ETMT experiment allowed the micro-texture formed during grain refinement to be directly correlated to the coarse prior parent β-grain orientations. This revealed that, following compression by 14% and rapid re-heating, each prior β grain developed a weakened texture characterised by a four-pole motif surrounding the prior {100} pole positions (Fig. 3). This unique texture was also consistent with the peak positions measured in the single parent β-grain sample used for the in-situ SXRD experiments (Fig. 6) since the diffraction data showed that the new β orientations that formed on rapid re-heating lay within a ~ 30° angle from the prior parent β orientation present in the gauge section. The consistent appearance of symmetric intensity patterns across all the diffraction data suggests the characteristic micro-texture seen in the rapidly heated samples was formed by a crystallographic relationship to the parent grain orientation. Furthermore, in the in-situ SEM heating experiments, which necessitated slow heating rates, β twins were revealed to emerge during heating. Fig. 8(e) and f display pattern quality EBSD maps for the in-situ experiment where β–β twin boundaries have been highlighted. It can be seen that at 900°C (43% β) two twin types – {332}<113> and {112}<111> – are present within the prior β grains and at their boundaries, although the {112}<111> twins dominate. It can also be noted that at 950°C, after most of the β–twin boundaries disappear, the newly nucleated β grains along the prior β grain boundaries almost all have {112}<111> type boundaries. Both of these twinning systems have been

observed occurring in metastable-β titanium alloys [45–47], but have not, to the authors' knowledge, been observed in Ti64. Deformation twinning is normally thought not to be favourable in the β phase in Ti64, and its composition does not lead to the formation of the $\omega$ phase that is believed to facilitate twinning in metastable β alloys [47]. However, it is possible that the fine microstructure generated as a result of the rapid cooling rate experienced by each added layer in AM may promote twinning of the β phase. For example, it has been found in nano-grained BCC alloys that, below a certain grain size, the critical stress required to activate deformation twinning drops dramatically [48]. The cause of this behaviour is believed to be due to the reduced probability of the presence of dislocation sources in a nanoscale-volume of material to facilitate slip [48,49]. This behaviour has most commonly been observed in FCC nano-grained materials [49,50], although it has recently also been confirmed to occur in nano-metals with BCC structures [48].

In order to see if β twinning could account for the micro-texture observed in Fig. 5 and the highly refined grain structures seen in Fig. 3 (a), parent grain reorientations arising from known BCC twinning operations were simulated [51], both individually and in combination, using a single original measured β orientation (i.e. with a measured texture spread following deformation). An example of this analysis is provided in Fig. 9 showing all the possible outcomes of different twinning operations, using the starting grain orientation in Fig. 5. From comparison of the simulations with the measured texture, it can be seen that a double twinning operation by the {112}<111> system produces a pole figure intensity distribution that most closely resembles the micro-texture found for the refined grains in the ETMT sample in Fig. 3(a). For clarity, the single to double twin orientation development by this system is provided more fully in Fig. 10. The operation results in 12 new possible unique orientations that have similar symmetry to that observed in Fig. 5. The parent and double-twinned orientations are compared in Fig. 9(a) and (d). In addition, it can be seen in Fig. 9(e) that the 12 modelled unique twin orientations closely match the experimental texture data (Fig. 9(f)); and with an assumed orientation spread of 8°, the predicted twinning variants could account for ~ 90% of the orientations of the refined grains present in the ETMT sample (Fig. 9(g)). A significant spread is also seen in the measured textures from the predicted ideal twin variant pole positions in Fig. 9(d), which can be accounted for by lattice rotation within the parent β grain caused by the deformation imparted before heating. Orientations that deviate from the twin relationship may also have nucleated from a BOR shared with twinned $\alpha$ present in the as-deformed material, a mechanism described in [27].

The double-twin operation modelled above also predicts the possibility for a given prior β orientation to first twin away and then back to its starting orientation. These returning orientations do not exist within the experimental results (coloured orange in the model in Fig. 9(g), compared to the refined region in Fig. 9(f)), and the contoured pole figure of the as-deformed and recrystallised β texture in Fig. 5 demonstrate that the propensity for these returning orientations to occur during double twinning is very low or non-existent. Since twinning occurs to better align a crystal to a preferential slip system or growth direction [52], a β grain is only likely to twin back to its starting orientation during a double-twinning operation if its neighbourhood constraints change mid-operation which, given the extremely short heating cycle time, is unlikely here. Thus, the original parent β texture does not survive the deformation-induced grain refinement, and the texture is continually weakened throughout a WAAM build height as more layers are deposited, deformed, and refined.

Although the new orientations generated by {112}<111> double twinning closely resembled the texture found in ex-situ EBSD maps (e.g. Figs. 5 and 7(b)) of the refined β grains in the process-simulated samples, in the in–situ SEM heating experiment (Fig. 8) only single twinning of the β was observed. In addition, many of the twinned regions within prior β grains disappeared as higher temperatures were reached. As noted above, this marked difference in behaviour is

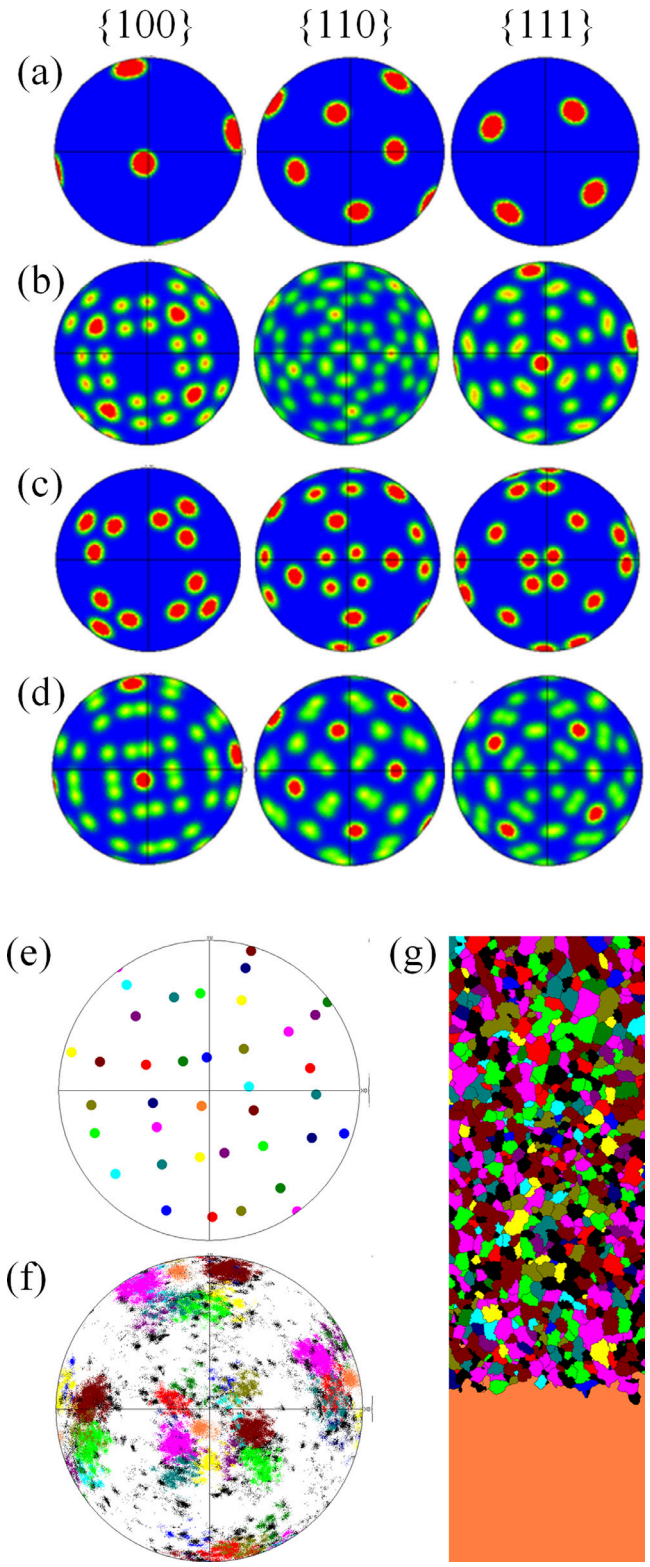



**Fig. 9.** Pole figures showing (a) the measured orientation used for the twinning simulations [51] taken from Fig. 5, and resultant pole figures of the orientations present after twinning a single orientation by the BCC twinning system by (b) {332}<113> once, (c) {112}<111> once, and (d) {112}<111> twice, assuming all twinning systems are activated. (e) shows the ideal 12 independent orientations obtained by twinning the parent β orientation in (a) by the {112}<111> twinning system twice, coloured individually in the {100} pole figure; and this colouring is continued into (f) and (g) where the non-contoured {100} pole figure and reconstructed-β orientation map of the region are given, respectively. Non-predicted orientations are coloured black in (f) and (g). (For interpretation of the references to colour in this figure legend, the reader is referred to the web version of this article.)

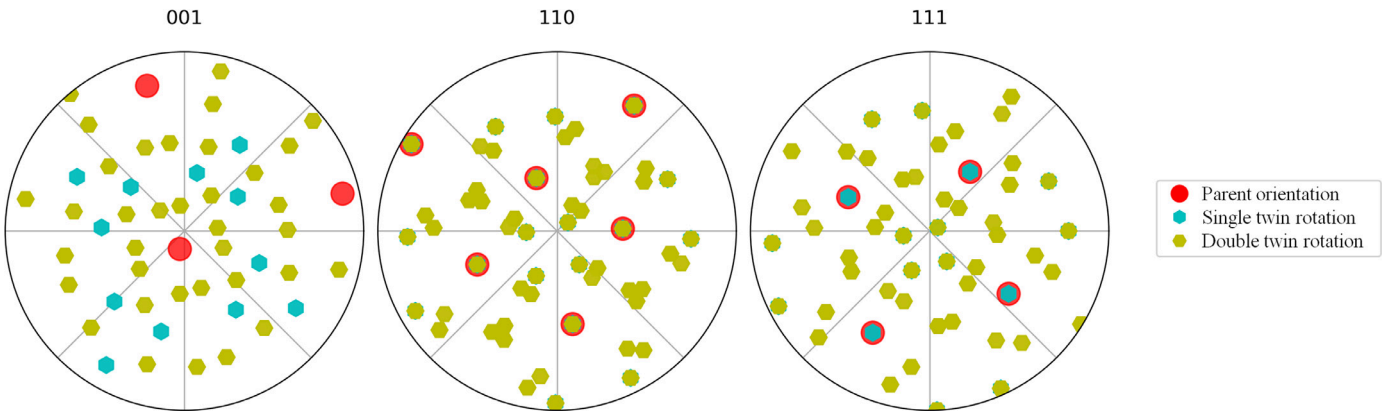



**Fig. 10.** Comparison of the simulated single and double {112}<111> twin operations using the starting ideal experimental orientation shown in Fig. 9(a). Twinning was simulated by rotating the parent orientation by 60° about the <111> directions [51].

most likely related to the much slower heating rates used in the in-situ SEM experiment, which were combined with isothermal holds at temperature to allow completion of the EBSD maps. This may have recovered much of the dislocation density provided by the prior deformation, so that the in-situ sample was far enough removed from the microstructural conditions experienced in a typical WAAM deformation and heating cycle to prevent the formation of double twins. In addition, since no β twins have been discovered in Ti64 previously, this strongly suggests their formation is uniquely related to the deformation and rapid heating conditions present in AM processes. However, it should also be noted that the in-situ experiment was carried out on a free surface, which would result in different constraining conditions on grains than would be experienced in a bulk sample.

Overall, the twin orientation calculations above have demonstrated that β-phase twinning is likely to be responsible for the high level of grain refinement and unusual micro-texture seen in the rapidly heated PSC samples, but what is not immediately clear, is if this arises from deformation or annealing; i.e. whether the twins originated during cold deformation, or during subsequent rapid heating through the β transus. In materials produced by WAAM, the room-temperature residual β in the microstructure is very fine, and it is thus difficult to determine the existence of deformation twins using standard characterisation techniques. To overcome this limitation, both high-resolution TKD and SPED orientation-mapping techniques were employed to attempt to identify twinning within the retained β in the deformed state, the results of which are depicted in Fig. 11. For these experiments, a sample was taken from the last added layer of the rolling-integrated WAAM wall in the area of highest strain. Even with an interaction volume of 12 $nm^3$, the TKD technique was still only able to index a relatively low β volume fraction of 0.5%. However, as can be seen in Fig. 11(a) and (b), of all the points indexed within a prior β grain only a single β orientation was found, with no twinning apparent. Reducing the interaction volume to ~ 3 $nm^3$ using SPED improved the indexing of the residual β to 5%, and a typical orientation map obtained with this method is shown in Fig. 11(c). In Fig. 11(d), the β phase has been separated from the $\alpha$ and it can be seen that the majority of β again has a single orientation, which is consistent with the TKD results. A very small fraction of indexed

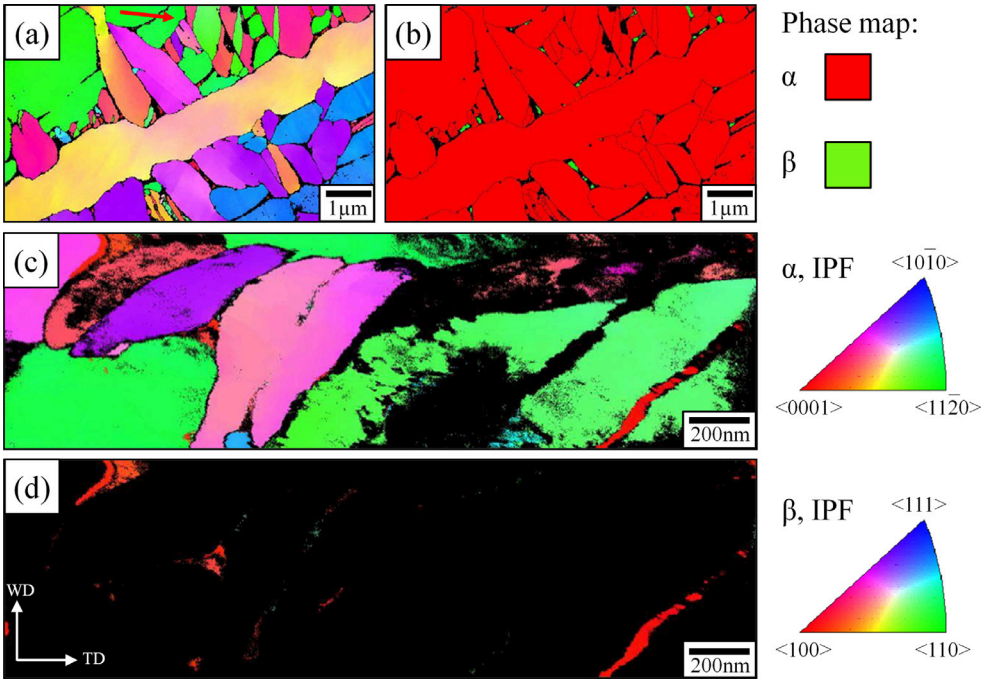



**Fig. 11.** Higher resolution orientation maps from the as-deformed microstructure in the rolled WAAM wall: (a) TKD orientation maps in IPF colouring with respect to the build direction, and (b) coloured by phase ($\alpha$ red, β in green) and (c)–(d) SPED orientations maps from the area arrowed in (a) displayed in (c) IPF colouring with respect to the build direction, and (d) same colouring but only β shown. (For interpretation of the references to colour in this figure legend, the reader is referred to the web version of this article.)

points were found with a second β orientation in the SPED data, although careful analysis of the diffraction patterns in question revealed this to be caused by systematic misindexing.

Therefore, overall, the application of both high-resolution techniques did not reveal the presence of any pre-existing β deformation twins prior to re-heating. Unfortunately, despite this analysis, the existence of deformation twining cannot yet be completely dismissed because of the limited sample volume available from FIB preparation.

Compared to deformation twinning, the evidence for annealing twins is more convincing. The rapid heating SXRD results in Figs. 6 and 7 showed that new β orientations only appeared when the β volume fraction had increased from 76% to 92% β; that is, they formed during the latter stages of β re-growth on rapid heating toward the β transus. Conversely, if deformation twins were responsible for the new orientations, they would already have been present in the room-temperature microstructure and would be expected to be seen growing from the beginning of the transformation in the SXRD results; i.e., they would appear simultaneously with the increase in intensity of the prior β orientation from lower temperatures, which was not observed.

A schematic diagram of a suggested annealing-twin mechanism is depicted in Fig. 12 which shows the re-growth of residual β in a deformed (Fig. 12(a)) and undeformed (Fig. 12(b)) α+β lamellar microstructure. It is proposed that, during the α–β transformation, the presence of dislocations stored in the deformed lamellar microstructure triggers a *rare* twin-induced nucleation event within a residual β lamella as it re-grows into the surrounding α (Fig. 12(b)-(ii)). This strain-free recrystallised grain, with an orientation different to the parent grain (β'), then consumes the remainder of the deformed parent β orientation within the grain due to a growth advantage [52], while continuing to expand into the surrounding α along with the parent β (Fig. 12(b)-(iii)). The recrystallised β' grain remains separated from the parent deformed β, which dominates the microstructure, until the remaining α transforms to deformed β. With no α remaining, the twin re-orientated β' grain is no longer pinned and quickly consumes and eliminates the deformed prior β (Fig. 12(b)-(iii,iv)). The twinned grain then grows until it impinges upon other recrystallised grains forming the refined, equiaxed microstructure seen in the WAAM simulations in Fig. 3(a).

This sequences of events is consistent with the SXRD results in Fig. 7(a), which first show the prior β peak diffraction intensity increasing as the α phase initially shrinks, before new β orientations appear (with a misorientation consistent with twinning) and grow

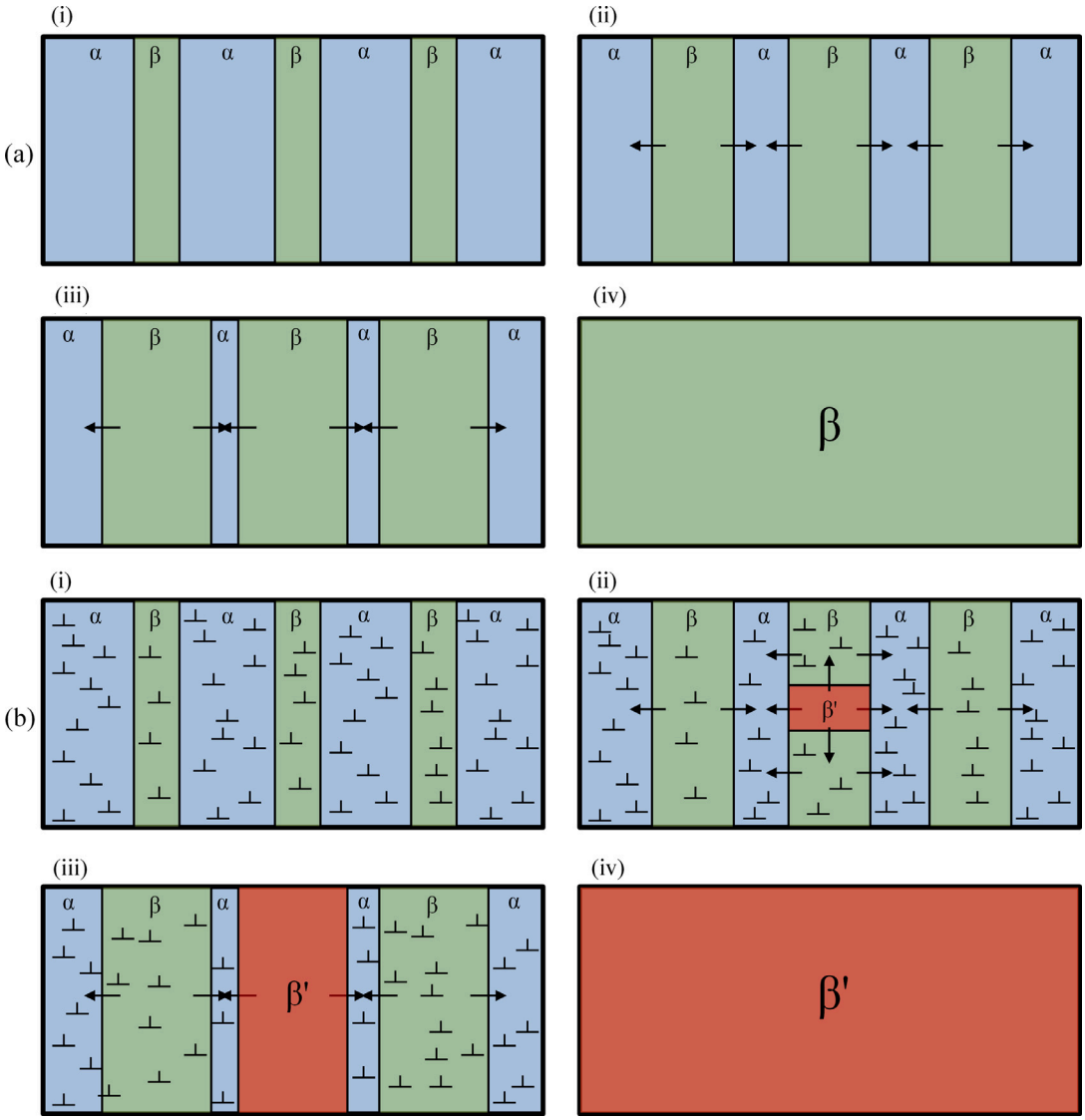



**Fig. 12.** A schematic diagram of a possible annealing twin recrystallisation mechanism that can operate during rapid heating of a deformed lamellar α-β microstructure: (a) shows thin, strain-free, inter-lamellar residual β, surrounded by strain-free α, which transforms to β upon heating to dominate the microstructure; and (b) shows the same situation in the presence of deformation (b)-(i) whereby, upon heating, a strain-free β annealing twin forms (β') during the α-β transformation and, whilst constrained by the remaining α, consumes the parent deformed β (ii–iii); then, after the remaining α has transformed, the β' consumes the surrounding transformed deformed parent β orientation (iv).

simultaneously with the prior β. This continues until the last 10% of the transformation when the prior β orientation starts to rapidly diminish as the new twinned β orientations continue to grow, consuming the original prior parent β orientation. In addition, no diffraction intensity from the prior parent β orientation was found in the final β-reconstructed texture of the SXRD sample (Fig. 7(b)) confirming that all of the prior β orientation was consumed during the final stage of the heating cycle to be replaced by the twin-related variants simulated in Fig. 9; i.e., if conventional recrystallisation had occurred, some remnant or orientation spread related to the original parent grain would have been expected to still be present.

The twin simulations indicated that the unique four-pole motif micro-texture seen in this study can only be replicated by *double* twinning of the {112}<111> system, and not by a *single* twinning operation as presented in the simplified mechanism discussed above. This disparity could be explained by the double-twinned β grains obtaining an energetically favourable growth direction during the recrystallisation and competitive growth process. However, due to the extremely short time span in which the proposed twinning may occur, this mechanism could not be confirmed experimentally and will instead be investigated further using modelling techniques in a following publication.

It should be taken into account that the simulation experiments in this work were conducted on a coarse columnar β-grain structure taken from an unrolled WAAM wall and are not entirely representative of the grain refinement conditions occurring in the inter-pass rolling WAAM process. In the real process, the grain structure is refined incrementally by rolling each layer as it is added and is not allowed to develop into such a coarse starting columnar structure before it is deformed. For example, the last layer deposited in the inter-pass rolled WAAM wall is highlighted in Fig. 1(c) and consists of much smaller columnar grains with a grain diameter of ~ 350 $\mu$m and a less developed solidification texture. In the actual WAAM process, the cyclic deformation and β refinement that occurs incrementally as each layer is sequentially added, deformed, and re-heated, is thus also an important factor in why inter-pass rolling is so effective in refining the β-grain structure in the WAAM process [18].

Finally, it should be noted that this research has wider implications than high deposition rate AM, as coarse grain structures and texture colonies are a common issue in many titanium products. Traditionally, deformation processing of Ti64 is carried out at high temperatures due to the high flow stresses and large strains required to break up the large, prior β structure formed on casting, and in sub-transus deformation under conditions where there is a coarse $\alpha$-β microstructure. The discovery of a new mechanism for β refinement, requiring relatively small strains at low temperatures could have wider applicability than just AM, although, exploitation would be difficult in all but small-section Ti64 products, as both the cooling rates required to generate the fine $\alpha$ microstructure, and the forces required to plastically deform the material at room temperature, would be prohibitively difficult to achieve in a large billet. However, owing to its incremental nature, directed energy deposition additive manufacture is particularly suited to taking advantage of this mechanism, even when manufacturing large components. This includes the ability to both deform each layer and achieve the necessary rapid heating and cooling rates required for the twinning mechanism to operate, to limit β-grain growth, and to form a fine enough starting transformation microstructure.

## 5. Conclusions

A high level of β-grain refinement and textural weakening has been observed in wire-based additive manufacture when a low strain inter-pass rolling step is introduced into the process. To explain the origin of this interesting behaviour, we have successfully replicated the refined microstructure by simulating the deformation and the temperature profile experienced by each added and deformed layer. In-situ simulations were also conducted with high-flux SXRD to determine in real time, with matching heating rates, the growth dynamics of the prior β and new β orientations during rapid re-heating. In addition, EBSD mapping was performed in SEM in-situ heating experiments to just below the β transus, using a deformed WAAM sample, in order to directly observe the nucleation and growth of new β orientations and their relationship to the deformed microstructure.

Process simulation resulted in a similar, refined, equiaxed β-grain structure with an average grain diameter of ~ 50 $\mu$m, which was slightly finer than seen in rolled-WAAM builds (~ 80–100 $\mu$m [18]) and possessed a decidedly weakened texture. However, only a small set of process parameters were simulated in this work and such a refined grain structure is not seen in WAAM components owing to the greater amount of grain growth that occurs, due to the higher temperatures experienced on re-heating above the β transus. The process-simulated refined β grains bore a high symmetry orientation relationship to their prior coarse parent β grains, which produced a distinct, unique, weaker micro-texture represented by a four-pole motif centred on the parent {100} positions. This unusual texture has been related back to the parent grain orientation, by double twinning via the {112}<111> β system. Twins of this type were also observed in-situ by EBSD mapping in the rolled AM microstructure upon β re-growth when re-heating close to the β transus.

High-resolution orientation mapping by TKD and SPED were unable to identify β twins present in the as-deformed fine retained β phase. The SXRD results also showed that the new β orientations only started to appear after the prior β had already nearly fully transformed. From this evidence, it is suggested that the generation of annealing twins during rapid reheating of the lightly deformed $\alpha$-β WAAM microstructure could be responsible for the grain refinement. A mechanism to explain this phenomenon was proposed whereby β annealing twins that form during the $\alpha$-β transformation obtain a growth advantage, during the consumption of $\alpha$, over the prior parent β grain orientation.

Since detrimental coarse grain structures are a problem in many titanium products, this discovery of a new β-refinement mechanism may be applicable to other titanium production processes than just AM.

## Declaration of Competing Interest

The authors declare that they have no known competing financial interests or personal relationships that could have appeared to influence the work reported in this paper.

The authors declare the following financial interests/personal relationships which may be considered as potential competing interests: No interests to declare.

## Acknowledgments

The authors are appreciative of the EPSRC grants (LightForm – EP/R001715/1; NEWAM – EP/R027218/1) and Innovate UK (Open Architecture Additive Manufacturing, OAAM) for supporting aspects of this research. Professor P.B. Prangnell is also grateful to the Royal Academy of Engineering, UK, and Airbus for financial support through the Airbus-University of Manchester Centre for Metallurgical Excellence.

## Supplementary materials

Supplementary material associated with this article can be found in the online version at doi:10.1016/j.actamat.2020.01.009.

## References


[1] J. Allen, An investigation into the comparative costs of additive manufacture vs. machine from solid for aero engine parts, in: Proceedings of the Meeting on RTO-MP-AVT-139, 2006, pp. 17-1–17-10.
[2] D.L. Bourell, Perspectives on additive manufacturing, Annu. Rev. Mater. Res. 46 (1) (2016) 1–18.
[3] D. Ding, Z. Pan, D. Cuiuri, H. Li, Wire-feed additive manufacturing of metal components: technologies, developments and future interests, Int. J. Adv. Manuf. Technol. 81 (1–4) (2015) 465–481.
[4] W.E. Frazier, Metal additive manufacturing: a review, J. Mater. Eng. Perform. 23 (6) (2014) 1917–1928.
[5] B. Baufeld, E. Brandl, O. Van Der Biest, Wire based additive layer manufacturing: comparison of microstructure and mechanical properties of Ti–6Al–4V components fabricated by laser-beam deposition and shaped metal deposition, J. Mater. Process. Technol. 211 (6) (2011) 1146–1158.
[6] K.M. Taminger, R.A. Hafley, Electron beam freeform fabrication for cost effective near-net shape manufacturing, Spec. Meet. Cost Eff. Manuf. Net Shape Process. (NATO/RTO AVT-139) 16 (2006) 1–10.
[7] J. Gockel, J. Beuth, K.M. Taminger, Integrated control of solidification microstructure and melt pool dimensions in electron beam wire feed additive manufacturing of Ti–6Al–4V, Addit. Manuf. 1 (2014) 119–126.
[8] F. Martina, P.A. Colegrove, S.W. Williams, J. Meyer, Microstructure of interpass rolled wire + arc additive manufacturing Ti–6Al–4V components, Metall. Mater. Trans. A Phys. Metall. Mater. Sci. 46 (12) (2015) 6103–6118.
[9] F. Martina, J. Mehnen, S.W. Williams, P.A. Colegrove, F. Wang, Investigation of the benefits of plasma deposition for the additive layer manufacture of Ti–6Al–4V, J. Mater. Process. Technol. 212 (6) (2012) 1377–1386.
[10] T. Duda, L.V. Raghavan, 3D metal printing technology, IFAC-PapersOnLine 49 (29) (2016) 103–110.
[11] A.R. McAndrew, et al., Interpass rolling of Ti–6Al–4V wire + arc additively manufactured features for microstructural refinement, Addit. Manuf. 21 (March) (2018) 340–349.
[12] J.R. Hönnige, et al., Residual stress and texture control in Ti-6Al-4V wire + arc additively manufactured intersections by stress relief and rolling, Mater. Des. 150 (2018) 193–205.
[13] C. Körner, Additive manufacturing of metallic components by selective electron beam melting – a review, Int. Mater. Rev. 61 (5) (2016) 361–377.
[14] T. DebRoy, et al., Additive manufacturing of metallic components – Process, structure and properties, Prog. Mater. Sci. 92 (2018) 112–224.
[15] I.A. Roberts, C.J. Wang, R. Esterlein, M. Stanford, D.J. Mynors, A three-dimensional finite element analysis of the temperature field during laser melting of metal powders in additive layer manufacturing, Int. J. Mach. Tools Manuf. 49 (12–13) (2009) 916–923.
[16] V.D. Fachinotti, A. Cardona, B. Baufeld, O. Van Der Biest, Finite-element modelling of heat transfer in shaped metal deposition and experimental validation, Acta Mater. 60 (19) (2012) 6621–6630.
[17] X. Bai, et al., Numerical analysis of heat transfer and fluid flow in multilayer deposition of PAW-based wire and arc additive manufacturing, Int. J. Heat Mass Transf. 124 (2018) 504–516.
[18] J. Donoghue, A.A. Antonysamy, F. Martina, P.A. Colegrove, S.W. Williams, P.B. Prangnell, The effectiveness of combining rolling deformation with wire-arc additive manufacture on β-grain refinement and texture modification in Ti–6Al–4V, Mater. Charact. 114 (2016) 103–114.
[19] P. Åkerfeldt, M.L. Antti, R. Pederson, Influence of microstructure on mechanical properties of laser metal wire-deposited Ti–6Al–4V, Mater. Sci. Eng. A 674 (2016) 428–437.
[20] F. Wang, S.W. Williams, P.A. Colegrove, A.A. Antonysamy, Microstructure and mechanical properties of wire and arc additive manufactured Ti–6Al–4V, Metall. Mater. Trans. A Phys. Metall. Mater. Sci. 44 (2) (2013) 968–977.
[21] A. Kumar, T. Jayakumar, B. Raj, D. Banerjee, A new methodology for identification of β-transus temperature in α + β and β titanium alloys using ultrasonic velocity measurement, Philos. Mag. 88 (3) (2008) 327–338.
[22] A. Ho, H. Zhao, J.W. Fellowes, F. Martina, A.E. Davis, P.B. Prangnell, On the origin of microstructural banding in Ti–6Al–4V wire-arc based high deposition rate additive manufacturing, Acta Mater. 166 (2019).
[23] M.J. Bermingham, S.D. McDonald, M.S. Dargusch, D.H. St.John, Grain-refinement mechanisms in titanium alloys, J. Mater. Res. 23 (1) (2008) 97–104.
[24] D.A. Porter, K.E. Easterling, Phase Transform. Metals Alloys 3 (1992).
[25] M. Rappaz, S.A. David, J.M. Vitek, L.A. Boatner, Analysis of solidification microstructures in Fe–Ni–Cr single-crystal welds, Metall. Trans. A 21 (6) (1990) 1767–1782.
[26] A.A. Antonysamy, J. Meyer, P.B. Prangnell, Effect of build geometry on the β-grain structure and texture in additive manufacture of Ti6Al4V by selective electron beam melting, Mater. Charact. 84 (2013) 153–168.
[27] J. Donoghue, A. Gholinia, J. Quinta da Fonseca, P.B. Prangnell, In-situ high temperature EBSD analysis of the effect of a deformation step on the alpha to beta transition in additive manufactured Ti–6Al–4V, TMS Titan. (2015) 1283–1288.
[28] S.S. Al-Bermani, M.L. Blackmore, W. Zhang, I. Todd, The origin of microstructural diversity, texture, and mechanical properties in electron beam melted Ti-6Al-4V, Metall. Mater. Trans. A Phys. Metall. Mater. Sci. 41 (13) (2010) 3422–3434.
[29] G. Lütjering, J.C. Williams, Titanium, Springer, 2007.
[30] K. Muszka, M. Lopez-Pedrosa, K. Raszka, M. Thomas, W.M. Rainforth, B.P. Wynne, The impact of strain reversal on microstructure evolution and orientation relationships in Ti–6Al–4V with an initial alpha colony microstructure, Metall. Mater. Trans. A Phys. Metall. Mater. Sci. 45 (13) (2014) 5997–6007.
[31] P.A. Colegrove, J. Donoghue, F. Martina, J. Gu, P.B. Prangnell, J.R. Hönnige, Application of bulk deformation methods for microstructural and material property improvement and residual stress and distortion control in additively manufactured components, Scr. Mater. 135 (2017) 111–118.
[32] P.A. Colegrove, et al., Microstructure and residual stress improvement in wire and arc additively manufactured parts through high-pressure rolling, J. Mater. Process. Technol. 213 (10) (2013) 1782–1791.
[33] F. Martina, S.W. Williams, P.A. Colegrove, Improved microstructure and increased mechanical properties of additive manufacture produced Ti-6Al-4V by interpass cold rolling, SFF Symp. (2013) 490–496.
[34] B. Roebuck, D.C. Cox, R.C. Reed, An innovative device for the mechanical testing of miniature specimens of superalloys, Tms 2004 (2004) 523–528.
[35] J. Filik, et al., Processing two-dimensional X-ray diffraction and small-angle scattering data in DAWN 2, J. Appl. Crystallogr. 50 (3) (2017) 959–966.
[36] M. Basham, et al., Data Analysis WorkbeNch (DAWN), J. Synchrotron Radiat. 22 (2015) 853–858.
[37] A.A. Coelho, J. Evans, I. Evans, A. Kern, S. Parsons, The TOPAS symbolic computation system, Powder Diffr. 26 (S1) (2011) S22–S25.
[38] G.A. Sargent, K.T. Kinsel, A.L. Pilchak, A.A. Salem, S.L. Semiatin, Variant selection during cooling after beta annealing of Ti–6Al–4V ingot material, Metall. Mater. Trans. A Phys. Metall. Mater. Sci. 43 (10) (2012) 3570–3585.
[39] P.S. Davies, An investigation of microstructure and texture evolution in the Near-α titanium alloy Timetal 834, University of Sheffield, 2009.
[40] P.S. Davies, B.P. Wynne, W.M. Rainforth, M.J. Thomas, P.L. Threadgill, Development of microstructure and crystallographic texture during stationary shoulder friction stir welding of Ti–6Al–4V, Metall. Mater. Trans. A Phys. Metall. Mater. Sci. 42 (8) (2011) 2278–2289.
[41] M. Humbert, N. Gey, The calculation of a parent grain orientation from inherited variants for approximate (b.c.c.-h.c.p.) orientation relations, J. Appl. Crystallogr. 35 (4) (2002) 401–405.
[42] N. Gey, M. Humbert, Specific analysis of EBSD data to study the texture inheritance due to the β→α phase transformation, J. Mater. Sci. 38 (6) (2003) 1289–1294.
[43] R.R. Keller, R.H. Geiss, Transmission EBSD from 10 nm domains in a scanning electron microscope, J. Microsc. 245 (3) (2012) 245–251.
[44] E.F. Rauch, L. Dupuy, Rapid spot diffraction patterns identifiction through template matching, Arch. Metall. Mater. 50 (1) (2005) 87–99.
[45] Y. Yang, et al., Stress-introduced α″ martensite and twinning in a multifunctional titanium alloy, Scr. Mater. 58 (1) (2008) 9–12.
[46] E. Bertrand, P. Castany, I. Péron, T. Gloriant, Twinning system selection in a metastable β-titanium alloy by Schmid factor analysis, Scr. Mater. 64 (12) (2011) 1110–1113.
[47] S. Hanada, O. Izumi, Transmission electron microscopic observations of mechanical twinning in metastable beta titanium alloys, Metall. Trans. A1 17 (1986) 1409–1420.
[48] J. Wang, Z. Zeng, C.R. Weinberger, Z. Zhang, T. Zhu, S.X. Mao, In situ atomic-scale observation of twinning-dominated deformation in nanoscale body-centred cubic tungsten, Nat. Mater. 14 (6) (2015) 594–600.
[49] Y.T. Zhu, X.Z. Liao, X.L. Wu, J. Narayan, Grain size effect on deformation twinning and detwinning, J. Mater. Sci. 48 (13) (2013) 4467–4475.
[50] H.S. Park, K. Gall, J.A. Zimmerman, Deformation of FCC nanowires by twinning and slip, J. Mech. Phys. Solids 54 (9) (2006) 1862–1881.
[51] J. Quinta Da Fonseca, "LightForm-group/cubic-twinning-model: twinning re-orientation calculations." 2019.
[52] F.J. Humphreys, M. Hatherly, Recrystallization and Related Annealing Phenomena, Elsevier, Oxford, 1996.



https://dspace.org/

# On the observation of annealing twins during simulating -grain refinement in Ti–6Al–4V high deposition rate AM with in-process deformation

**Donoghue, Jack; Davis, Alec E.; Daniel, Christopher S.; Garner, Alistair; Martina, Filomeno ...**

**2020-01-08**
Elsevier
https://doi.org/10.1016/j.actamat.2020.01.009
Donoghue J, Davis A, Daniel C, et al., (2020) On the observation of annealing twins during simulating -grain refinement in Ti–6Al–4V high deposition rate AM with in-process deformation. Acta Materialia, Volume 186, March 2020, pp. 229-241

Downloaded from a DSpace repository. https://dspace.org/